# Length Dependent Photocatalytic Activity of Hybrid

# Ag-CdS Nanorods

Yongchen Wang,<sup>1</sup> Hawi N. Nyiera,<sup>1</sup> Ann W. Mureithi,<sup>1</sup> Yonglei Sun,<sup>2</sup> Tomoyasu Mani,<sup>1</sup> Jing Zhao<sup>1,2</sup>\*

<sup>1</sup>Department of Chemistry, University of Connecticut, 55 North Eagleville Rd, Storrs Mansfield, 0CT, 06269-3060, USA

<sup>2</sup>Institute of Materials Science, University of Connecticut, 97 North Eagleville Rd., Storrs Mansfield, CT 06269-3137, USA

KEYWORDS metal-semiconductor, silver, cadmium sulfide, nanorods, photocatalysis, charge transfer, dye degradation

ABSTRACT Hybrid metal-semiconductor nanostructures are promising photocatalysts for a widespan of reactions. Determining the relationship of their geometry with catalytic efficiency is critical for optimization of the catalysts. In this work, Ag-CdS nanorods with five different lengths (from 25.0 nm to 106.5 nm) have been synthesized using a seed-mediated growth method. High-resolution transmission electron microscopy (HRTEM) and energy dispersive X-ray spectroscopy (EDS) studies confirmed that the formation of a metal tip and semiconductor body part and they

absorbs strongly and broadly in the UV and visible wavelength range. The nanorods have been employed as photocatalysts for methyl orange degradation and their catalytic efficiency exhibited length-dependence. Specifically, highest efficiency was observed in the rods of intermediate length (72.1 nm). Time-dependent photoluminescence decay revealed that the Ag-CdS rods with high catalytic efficiency have higher probability to go through charge-separation and recombination pathway than the rods with low catalytic efficiency. Understanding the physical processed in these hybrid structures provides insight into fine tuning their geometry to improve the charge transfer efficiency from metal to semiconductor domain. Thus, better hybrid nanomaterials can be designed and fabricated for photocatalytic and other applications.

#### INTRODUCTION

Semiconductor metal oxides and chalcogenides have been studied and applied as photocatalysts for more than five decades<sup>1,2</sup>. During a photocatalytic reaction, an electron in the valence band of semiconductor is excited by light and moves into its conduction band, leaving a hole in the valence band. The excited electrons and holes subsequently diffuse to the surface of the semiconductor catalyst and are then consumed in reduction or oxidation reactions.<sup>3</sup> In order for the photocatalytic reaction to proceed, the semiconductor has to efficiently absorb light and the energy level of its conduction band and valence band have to be appropriate considering the redox potential of the reactants and the type of reaction<sup>2</sup>. The most commonly used semiconductor photocatalyst is TiO<sub>2</sub> due to its good stability at different pHs, nontoxicity, and commercial availability<sup>4</sup>. However, it can only absorb ultraviolet light and a small portion of visible light (4-8% of the solar spectrum) due to its large band gap<sup>5</sup>. To increase light utilization efficiency, a narrow bandgap

semiconductor is desired, which allows efficient absorption of visible light<sup>6,7</sup>. Moreover, charge transfer from the semiconductor to reactants has to compete with fast radiative and non-radiative recombination processes within the semiconductor<sup>8</sup>. These competing processes significantly lower the catalytic efficiency of semiconductors.

An effective way to suppress rapid charge recombination in the semiconductors is to combine a semiconductor with a metal cocatalyst. In hybrid metal-semiconductor nanostructures, a Schottky barrier forms at the metal-semiconductor interface if the metal's Fermi level is properly aligned with the semiconductor's valence band and conduction band. Photoinduced charge separated state could form after excitation where the excited electron in the semiconductor domain migrates to the metal, leaving the hole in the semiconductor. Because the Schottky barrier facilitates trapping of the photoexcited charge carriers<sup>9</sup>, this spatial separation of electrons and holes lengthens the lifetime of charge-separated states and therefore facilitate light-assisted oxidation/reduction reactions 10,11. This unique feature makes hybrid metal and semiconductor nanostructures attractive materials for photocatalysis. So far, a number of hybrid metal-semiconductor nanostructures with various metal and semiconductor components have been designed and constructed 10-14. In addition, the morphologies of them were fine-tuned to regulate their optical and electrical interactions, and their catalytic efficiency <sup>12,15–18</sup>. For example, Amirav et al. demonstrated that in a CdSe/CdS-Pt nanorods system, longer rods produced higher hydrogen generation quantum yields than shorter ones due to superior spatial charge separation and reduced back recombination<sup>19</sup>. It is critical to determine the impact of morphology of the nanomaterials on light-induced physical processes in hybrid nanostructures for efficient photocatalysts, solar cells, photoelectric devices, and biological labeling design<sup>20</sup>.

In an effort to understand how the length of metal-semiconductor nanorods affects their catalytic and optical properties, we synthesized Ag-CdS nanorods with five different lengths using a seed-mediate growth method. High-resolution transmission electron microscopy (HRTEM) and energy dispersive X-ray spectroscopy (EDS) studies confirm that the nanorods are composed of a metal tip and an elongated semiconductor domain. The nanorods were employed as photocatalysts for methyl orange degradation. The catalytic performance of the nanorods depends on the rod length, but not in a monotonic manner. Steady state and time-dependent photoluminescence (PL) of the nanorods were collected and compared to that of rod-like CdS nanoparticles. A slow decay component was observed in the PL decays of the Ag-CdS nanorods but not in the rod-like CdS nanoparticles, due to the formation of a charge-separated state. We discovered that the proportion of photons emitted from the charge-separated state correlates to the catalytic efficiency of the Ag-CdS nanorods.

#### **EXPERIMENTAL SECTION**

#### Chemicals and Materials

Cadmium oxide (>99.99%), oleic acid (technical grade, 90%), 1-octadecene (ODE, technical grade, 90%), silver nitrate, sulfur powder, methyl orange, hexane and oleylamine (70%) were obtained from Sigma-Aldrich. Trioctylphosphine oxide (TOPO, ~99%) was purchased from Fisher Scientific. Ethanol (200 proof) was purchased from J.T.Baker. All chemicals were used as obtained without any purification.

Preparation of Ag Seeds and Post-Synthesis Size Selection

Ag seeds were prepared following published protocols with some minor changes<sup>21,22</sup>. Typically, 10.0 mL of oleylamine and 400 mg of silver nitrate (2.35 mmol) were mixed and degassed for 15 minutes at room temperature in a three-neck flask. The temperature of the mixture was then increased to 200 °C and maintained for 25 minutes. During this process, silver nitrate was reduced in the presence of oleylamine to form Ag nanoparticles. The reaction mixture was then cooled to 80 °C. 5.0 mL of hexane and 30.0 mL of ethanol was added to the reaction mixture, followed by centrifugation for 5 minutes at 5000 rpm. The precipitate was collected and added into 15.0 mL of hexane. After sonication, the solution was centrifuged for 8 min at 7000 rpm. Following that, the precipitate was collected and 5.0 mL of hexane was added to it. The solution was then centrifuged at 5000 rpm for 5 minutes after sonication. Lastly, the precipitate was dispersed in hexane and the solution was filtered with a 0.22 μm Millipore syringe filter. The samples were kept in hexane until further usage (1.0 mg/mL).

## Synthesis of Hybrid Ag-CdS Nanorods

Cadmium oleate was used as the cadmium precursor for the formation of CdS nanorods. The synthesis of 0.2 M Cadmium oleate solution referred to a previous literature<sup>23</sup>. Typically, cadmium oxide (0.2568 g, 0.002 mol), oleic acid (3.8 mL), TOPO (0.3 g), and ODE (6.2 mL) were mixed in a flask. The mixture was heated and degassed under vacuum until it reached 100 °C. The mixture was then heated to 180 °C for 10 minutes under nitrogen flow to get a clear solution. Sulfur precursor solution of 0.2 M was made by dissolving 32 mg of sulfur powder (1 mmol) in 5 mL of oleylamine and sonication for 5 minutes. The sulfur precursor has to be prepared freshly prior to nanorod synthesis. The ratio of Cd and S precursors was kept to 1:1 for all the synthesis.

Ag-CdS nanorods with different lengths were obtained by the following protocol with varying ratios of Ag seeds to Cd and S precursors (see Figure 1). In a typical Ag-CdS nanorod synthesis, 1.0 mL of Ag seeds solution (concentration of 1.0 mg/mL) were placed into a three-neck flask and dried using nitrogen flow. We then dissolved the Ag seeds into 5.0 mL of oleylamine. The mixture was loaded into a three-neck flask and degassed for 10 minutes at room temperature. The

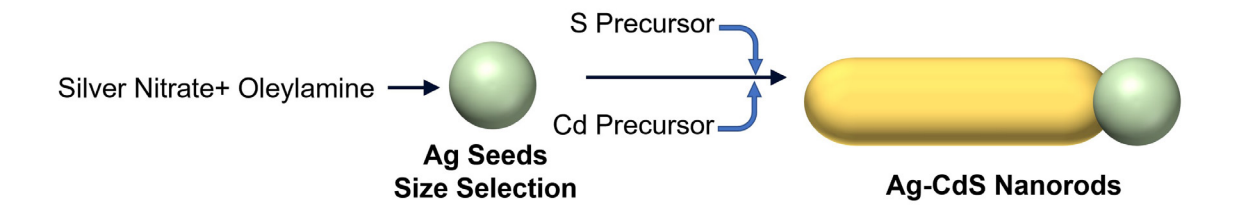


Figure 1. Illustration of the seed-mediated Ag-CdS nanorod synthesis.

temperature was elevated to 160 °C, and 0.5 mL sulfur and 0.5 mL cadmium precursors were injected at the same time. The reaction mixture was kept at 160 °C for 5 min under magnetic stirring and nitrogen protection. The solution was cooled to 80 °C and ethanol was added, followed by centrifugation at 6000 rpm for 2 minutes twice. The resulting precipitate was weighed and dispersed in hexane at 1.0 mg/mL concentration for further analysis. The protocol described here yielded Ag-CdS nanorods with an average length of 93.9 nm of the CdS domain as revealed by transmission electron microscopy (TEM). The length of the Ag-CdS can be controlled by varying the Ag:Cd(S) ratio, which will be discussed in detail later.

# Photocatalytic Methyl Orange Degradation

The photocatalytic activity of the Ag-CdS nanorods for methyl orange degradation was evaluated as the following. Briefly, 1.5 mL (1.5 mg) of Ag-CdS nanorod sample in hexane was taken and mixed with 4.5 mL of ethanol, followed by centrifuging at 6000 rpm for 2 min. 1 mL of ethanol

was then added to the precipitate. The mixture was sonicated and transferred into a UV-plastic cuvette containing 2 mL of ethanol. The Ag-CdS nanorod ethanol solution was stirred under the radiation of a blue LED lamp (450-460 nm) for 30 minutes. After irritation, 150 μL of 1.0 mM methyl orange ethanol solution was added into the cuvette and capped. The reaction mixture was radiated by the same blue LED lamp for desired durations. 100 μL of the mixture was taken for analysis each time at varied reaction times and added to 1.0 mL of ethanol. The nanorods were then removed by centrifugation at 6000 rpm for 5 minutes. The precipitate was discarded and the supernatant was analyzed by UV-vis spectroscopy.

#### Characterization Instruments

The absorption spectra of the nanorods and the reactants were measured using an ultraviolet-visible (UV-Vis) spectrometer (Cary 60, Agilent technologies). Photoluminescence spectra of the nanorods were measured with a Horiba Fluoromax Plus Fluorometer. Transmission electron microscopy (TEM) images, and high angle annular dark field microscopy-scanning transmission electron microscopy (HAADF-STEM) images were obtained using FEI-Talos microscope operated at an accelerating voltage of 200 kV. The energy dispersive X-ray spectroscopy (EDS) detector mounted to the FEI Talos microscope was used for elemental analysis. Fluorescence lifetime measurements were performed using a TCSPC system of a FLS1000 (Edinburgh Instruments) equipped with a TCSPC/MCS/counter module (TCC2), a Hamamatsu H10720-01P, and a pulsed 405 nm diode laser (EPL-405) as the excitation source with a pulse duration of 55 ps. Fitting of datasets was carried out using FAST (Edinburgh Instruments).

# **RESULTS AND DISCUSSION**

As illustrated in Figure 1, the hybrid Ag-CdS nanorods were synthesized via a two-step seed-mediated growth, where the diameter of the nanorods is dictated by the diameter of the Ag

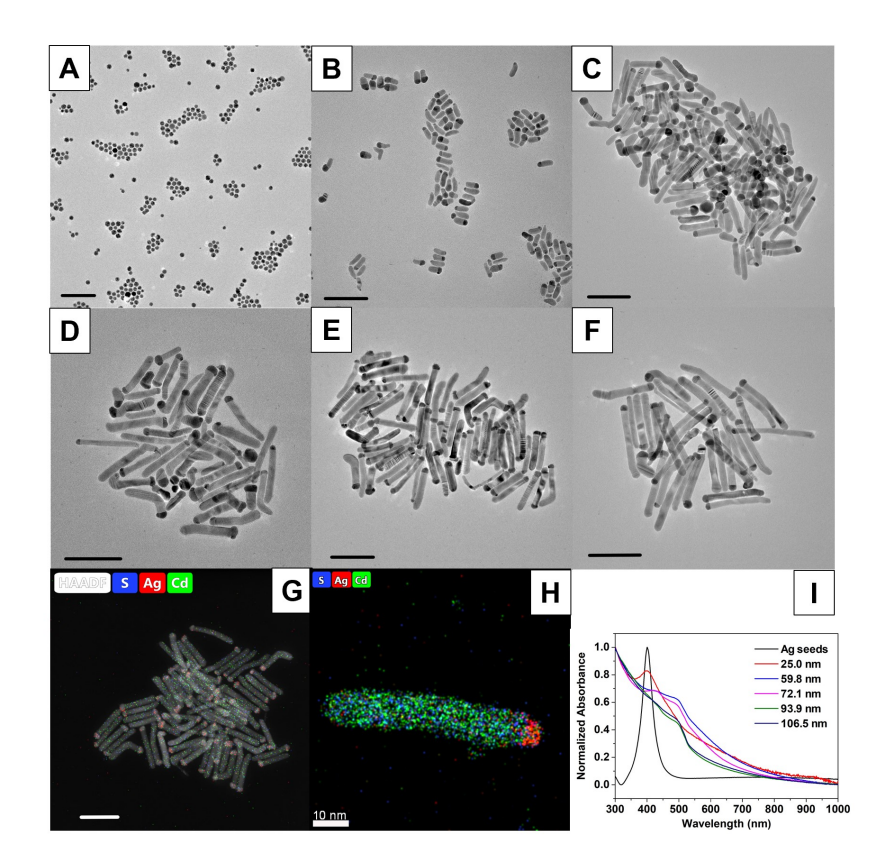


Figure 2. TEM images, HAADF-STEM image and UV-vis spectra of Ag seeds and Ag-CdS nanorods. A) Ag seeds with a diameter of  $13.2 \pm 1.9$  nm. B-F) Ag-CdS nanorods with a rod length of B)  $25.0 \pm 5.7$  nm, C)  $59.8 \pm 15.4$  nm, D)  $72.1 \pm 30.9$  nm, E)  $93.9 \pm 10.4$  nm, F)  $106.5 \pm 17.8$  nm. Figure 2G shows a typical HAADF-STEM elemental mapping image of the Ag-CdS nanorods with a rod length of  $93.9 \pm 10.4$  nm. Figure 2H shows an elemental mapping image on a single nanorod. Ag is marked in red, while Cd in green and S in blue. All of the scale bars in Figure 2A to 2G are 100 nm. Scale bar in Figure 2H is 10 nm. I) UV-vis absorption spectrum of Ag seeds and hybrid Ag-CdS nanorods with five different lengths in hexane.

seeds. In order to obtain Ag seeds with good size uniformity, a post-synthesis size selection process

was adopted after the Ag seeds were formed. Comparing the TEM images of Ag seeds before (Figure S1) and after size selection (Figure 2A), the relative standard distribution of the sizes of Ag seeds improved from 29.4% to 14.3%. The average diameter of the selected Ag seeds was 13.2  $\pm$  1.9 nm and these seeds were used for the following Ag-CdS rod synthesis. All of the Ag seeds used in the next step were from the same batch after size selection.

In the second step, CdS nanorods were grown on the Ag seeds following the protocol detailed in the Experimental Section. The types of precursors, reaction time, and temperature were optimized to obtain hybrid Ag-CdS nanorods (see more details in SI). In order to control the length of the CdS domain, the ratio of the Ag:Cd(S) precursors were varied while keeping other reaction conditions the same. As shown in Table 1, the Ag:Cd(S) ratios were varied by tuning the amounts of the Ag seeds and Cd/S precursors. The moles of Cd and S were the same in all reactions. The final product was characterized by TEM and the rod lengths were carefully measured using ImageJ software. Note that the rod length discussed here is the length of the CdS domain only, which does not include the metal tip. The TEM and HAADF-STEM images of five samples were illustrated in Figure 2. The lengths of the CdS domain were measured to be B)  $25.0 \pm 5.7$  nm, C)  $59.8 \pm 15.4$ nm, D)  $72.1 \pm 30.9$  nm, E)  $93.9 \pm 10.4$  nm, F)  $106.5 \pm 17.8$  nm, respectively. Figure 2G and 2H showed typical HAADF-STEM elemental mapping image of the Ag-CdS nanorods with a rod length of  $93.9 \pm 10.4$  nm at a larger scale (2G) and of a single rod (2I). Ag signal is strictly confined in the metal tip part, while the rod part consists of Cd and S. Note that in Table 1, the average rod length was determined based on samples synthesized in several batches under the same conditions. The variation in the CdS rod length of the final product within each synthesis and among different trials may arise from the variations in the crystal facets and surfaces of Ag seeds, the uncertainty in the mass of the Ag seeds from the balance, and the unavoidable variations in the reaction

temperature from the instruments. Nevertheless, the method reported here allowed for the synthesis of Ag-CdS nanorods with various length; and the greater the Ag:Cd(S) ratio is, the shorter the rods are.

Table 1 Rod-length control by tuning the Ag:Cd(S) ratio during the synthesis

Ag seeds (mg)	Cd/S precursor (mmol)	Ag:Cd(S) ratio (mg/mmol)	Average CdS nanorod length (nm)
2.0	0.040	50	25.0
2.0	0.048	42	59.8
2.0	0.064	31	72.1
1.0	0.060	17	93.9
1.0	0.10	10	106.5

The normalized UV-Vis absorption spectra of the Ag seeds and hybrid Ag-CdS nanorods with five different lengths are shown in Figure 2I. The Ag seeds have a narrow and strong absorption peak around 410 nm. After the CdS were grown on the Ag seeds, the absorption band become broad due to the absorption of CdS. While absorption of the Ag seeds at ~ 410 nm is visible in the 25.0 nm rod sample; as rod length gets longer, the absorption of Ag becomes less distinguishable. The absorption of 93.9 nm and 106.5 nm sample is completely dominated by the absorption of CdS. Nevertheless, all of the samples have strong absorption in the 400-500 nm wavelength range; therefore, a 450-460 nm LED was used to excite the nanorods in the following photocatalysis experiments.

To evaluate the catalytic activities of the hybrid Ag-CdS nanorods, the nanorods were mixed with methyl orange in ethanol, and irradiated under the blue LED. UV-vis spectra of the

sample were taken at varying irradiation times. The concentration of methyl orange is proportional to the area of absorption band at ~ 450 nm. Surprisingly, the absorbance of methyl orange did not change for the first 10 minutes of irradiation (Figure S2A). In order to examine the effect of light on the nanorods, the Ag-CdS nanorod ethanol solution without methyl orange was irradiated under the blue LED for up to 60 minutes. A color change in the solution was noticed after irradiation (Figure S3A) for all the rod samples tested. The absorbance of the Ag-CdS nanorods ethanol solution before and after 10 minutes irradiation exhibit some change, as evident from the UV-vis

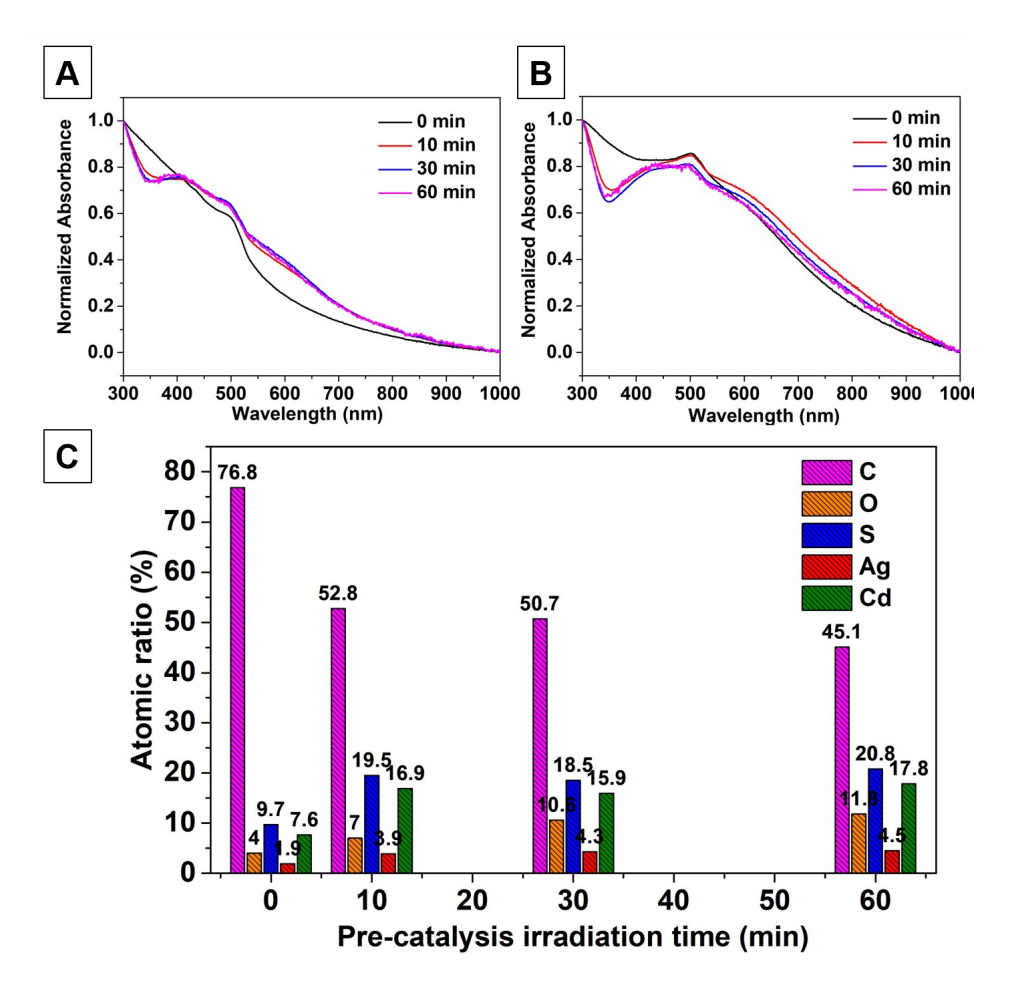


Figure 3. UV-vis spectra of Ag-CdS nanorods during the irradiation process A) rod length of 93.9 nm and B) rod length of 59.8 nm. C) Elemental analysis of Ag-CdS nanorods with 93.9 nm rod length using EDS.

spectra of two rod samples of different lengths in Figure 3A and 3B. The Ag-CdS nanorods of 93.9 nm length before and after irradiation for varying time were analyzed using HAADF-STEM. The elemental distribution of the rod sample at varying irradiation times was determined from EDS mapping analysis (Figure 3C). While the ratio between O, Ag, Cd and S were almost the same throughout all the samples, we observed a significant carbon percentage drop after 10 minutes of irradiation. Since carbon in the sample is mainly from the ligands (oleylamine), the decrease in carbon percentage in conjunction with the aggregation of the nanorods suggests that the ligands have dissociated from the rod surface. Similar light-induced ligand dissociation from Cd based nanoparticles were observed in our earlier work<sup>24</sup>. The ligand dissociation exposed the surface of the nanorods and made them more accessible for methyl orange. Therefore, the ~ 10 minutes "activation" phase for methyl orange is ascribed to ligand dissociation under irradiation. When the irradiation time was further increased, the degradation rate continued to increase for some samples and became stable at  $\sim 30$  mins and beyond (see details in the SI). Thus, all the catalysts were preirradiated for 30 mins before methyl orange addition to ensure that the degradation rates of nanorods with different lengths were not affected by the activation period.

The photocatalytic performance for methyl orange degradation was tested for Ag-CdS nanorod samples of five different lengths, and each sample was tested for at least three times. All the nanorod samples were irradiated under blue LED for 30 mins before methyl orange addition. The mass of the catalysts and the reaction conditions were kept the same in all the experiments.

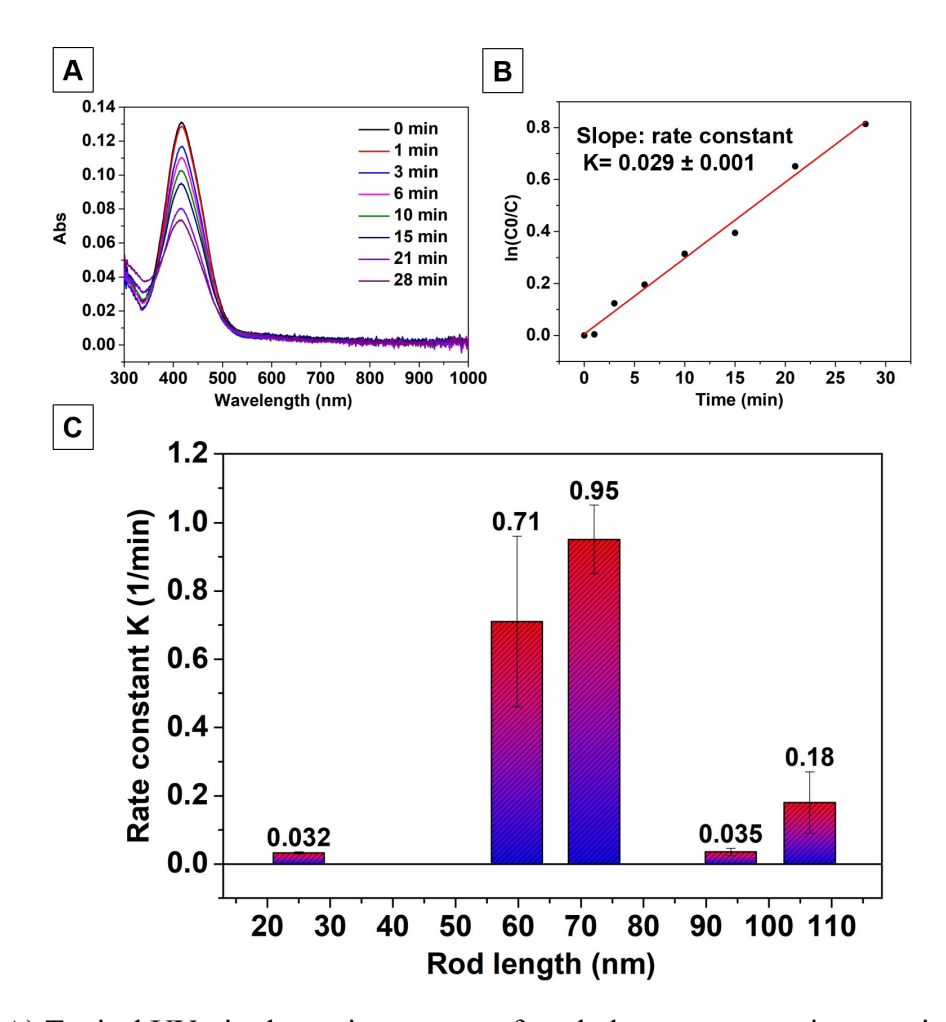


Figure 4. A) Typical UV-vis absorption spectra of methyl orange at varying reaction time; B) pseudo first-order rate constant determination; and C) rate constant of methyl orange degradation using Ag-CdS nanorods with five different lengths as photocatalyst.

After methyl orange addition, the mixture was irradiated under blue LED for varied time. 100  $\mu$ L of solution was taken from the reaction mixture during the reaction and centrifuged to remove the

nanorods. The UV-vis spectra of the supernatant were taken and plotted. Figure 4A shows an example of the UV-Vis absorption spectra of methyl orange at varying reaction times. The absorbance of methyl orange clearly decreased over time, confirming its degradation. Degradation does not occur without light when methyl orange was mixed with the nanorods, or when it was irradiated without nanorods. Since the area of the absorbance peaks is proportional to methyl orange concentration, the area ratio of the peaks to that at 0-min was used to represent the changes in methyl orange concentration. As revealed in previous studies, methyl orange degradation is a pseudo first order process<sup>25,26</sup> (Figure 4B). Same procedure was repeated three times and an average rate and standard deviation was calculated ( $log \frac{c_0}{c} = kt$ ) and plotted in Figure 4C. Comparing the five samples, the rate constant was rod-length dependent, but not in a monotonic way. The lowest rate constant was observed in the sample of 25.0 nm. The rate then increased when the rod length became longer and decreased again. The highest rate was observed in the 72.1 nm nanorod sample, which is 0.95 min<sup>-1</sup> on average. This value is 29 times higher than that of the 25.0 nm sample which showed an average rate constant of 0.032 min<sup>-1</sup> (Figure 4C). These results show the photocatalytic activity of Ag-CdS nanorods is length-dependent, and the nanorods of intermediate lengths show the highest activities. Also, we have tested the photocatalytic performance of the nanorods by collecting the catalysts after reaction and reusing them for four cycles. We did not observe any significant activity drop within the four cycles, confirming that the nanorods are stable and reusable.

In order to understand the physical processes in the nanorods after photoexcitation, we acquired steady state photoluminescence (PL) and time-dependent PL decay of the nanorods in hexane (Figure 5). Rod-like CdS nanoparticles (diameter of  $7.0 \pm 1.2$  nm and length of  $16.0 \pm 1.7$  nm) were also synthesized (see synthetic details in SI) and examined for comparison. Figure 5A

shows the PL spectra of rod-like CdS, and Ag-CdS nanorods with varying lengths excited at 400 nm. The PL spectrum of the rod-like CdS nanoparticles has a peak at 492 nm due to the band-edge emission and a very weak and wide bump at 665 nm due to trap-state emission. The assignment of the peaks is based on the similar spectral features reported in CdS quantum dots<sup>27,28</sup>. For the Ag-CdS nanorods, the band-edge emission become indistinguishable. Instead, they exhibit a broad emission feature in the range of 470-750 nm, peaked at 536-583 nm. We attribute this feature to three recombination processes illustrated in Figure 5C: exciton recombination, trap-state emission, and charge-separated state recombination. This emission feature is broader and more intense compared to the trap state emission of the rod-like CdS nanoparticles. One possible reason is that more traps formed during the longer nanorod growth. Moreover, since the length of the CdS domain in Ag-CdS nanorods is much longer than that of the rod-like CdS nanoparticles, excitons are less confined in the longitudinal direction of the rods, which would lower the bandgap according to quantum confinement in semiconductor nanocrystals<sup>29</sup>. Thus, a red-shift in emission is expected. Lastly, the charge-separated state refers to the state where excited electron migrates from CdS to Ag, leaving the hole in CdS. Since the Fermi level of Ag is lower than the energy level of the conduction band of CdS<sup>21</sup>, the recombination of the charge separated state will also lead to red-shifted emission.

To further evaluate the broad emission feature of Ag-CdS nanorods, time-dependent PL decay of these samples were collected at the peak wavelength for each sample and shown in Figure 5B. The PL decays were fitted with a commercial software FAST (Edinburgh Instruments) which calculates the PL lifetime distribution. The PL decay of rod-like CdS nanoparticles was well-fitted with a single exponential fitting with a lifetime of 0.82 ns. The PL decays of all the Ag-CdS nanorods have multiple components. For the samples with rod length of 25.0, 93.9 and 106.5 nm,

the decays are heavily weighted towards a fast decay component with a lifetime < 3 ns. But the samples with rod length of 59.8 and 72.1 nm have a significant slow component in their PL decays with a lifetime longer than 400 ns (see Tables S1-S5 for details of the fitting parameters). Although the fitting of the PL decays indicates that the physical processes in the Ag-CdS rods are complex, we attribute the major fast decay components (shaded in gray in Tables S1-S5) to the trap-state emission, since its lifetime is consistent with that of the rod-like CdS nanoparticles. Furthermore, the major slow decay components in the decays of 59.8 nm and 72.1 nm Ag-CdS nanorods (shaded in blue in Tables S1-S5) are attributed to the recombination of the charge-separated states, since the charge-separated states have been reported to be long-lived in metal-semiconductor

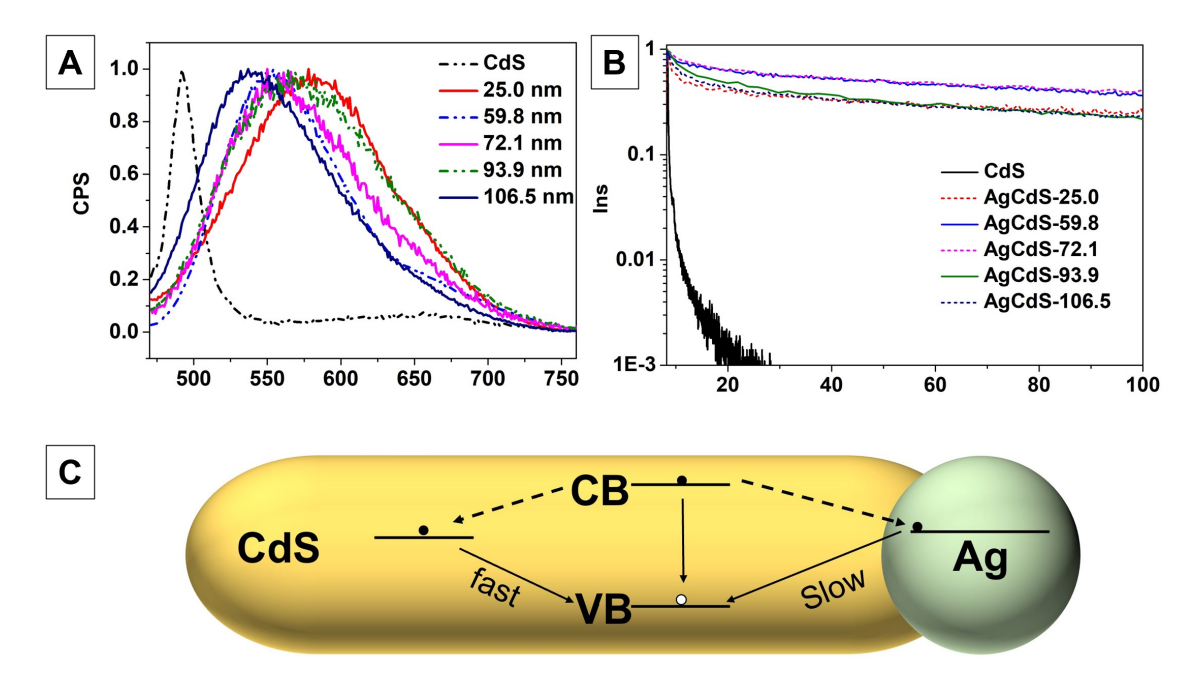


Figure 5. A) Steady state photoluminescence (PL) spectra and B) time-dependent PL decay of the Ag-CdS nanorods with different lengths in hexane. C) Schematic illustration of the possible exciton recombination processes.

nanostructures<sup>30</sup>. Note that the slow decays were found in the PL decays of 25.0 nm and 93.9 nm Ag-CdS nanorods as well, but their contribution towards the total photon emission is much smaller. The PL decay fitting results suggest that when excited, the Ag-CdS-59.8 nm and Ag-CdS-72.1 nm nanorods have higher probability to go through a charge-transfer process where the electron moves from CdS to Ag than Ag-CdS nanorods of other lengths. Thus, higher charge-separated state emission was observed in these two samples.

Charge-separated states in metal-semiconductor nanostructures are critical for their photocatalytic performance. Charge transfer from semiconductor to metal competes with the recombination within the semiconductor domain. Due to the long-lived nature of the chargeseparated state, it is more likely for the charges to be extracted from the metal-semiconductor catalysts for photocatalytic reactions than the semiconductor alone. Previous studies showed that photocatalytic methyl orange degradation involved formation of superoxide anion radicals and hydroxyl radicals which would both degrade the dyes in subsequent reactions<sup>31,32</sup>. The protons and dissolved oxygen could accept electrons from the charge-separated state of the photocatalyst, leading to the formation of these radicals, which has been reported in previous work on hybrid nanorods<sup>33</sup>. Meanwhile, the holes can be consumed by ethanol. Thus, extraction of charges from the photocatalysts is crucial and consequently influences the catalytic activity. For the Ag-CdS nanorods with varying rod-length, the length impacts the exciton lifetime, trap states, and likely the possibility of charge-transfer as well. Although the charge-transfer process in metalsemiconductor nanostructures typically happen at ultrafast time scale (picoseconds)<sup>30</sup>, it competes with charge-trapping and exciton recombination processes. The longer rod length leads to long exciton lifetime, slowing down exciton recombination. Meanwhile, longer rod length could also introduce more traps during growth, making trapping more likely to occur. The overall chargetransfer efficiency depends on the relative rates of charge-transfer, exciton recombination, and trapping, which does not lead to a monotonic increase in the charge-separated state emission of the Ag-CdS nanorods when increasing the rod length. Instead, the charge-separated state emission increases when the rod length increases from 25.0 nm to 59.8 nm then to 72.1 nm, and then decreases when rod length further increases to 93.9 and 106.5 nm. The trend agrees well with the photocatalytic efficiency of the nanorods (shown in Figure 4C). These results demonstrated that the charge-separated state is critical for the efficiency of photocatalytic reactions. Thus, when designing photocatalyst, it is desired to devise the geometry to optimize the formation of charge-separated states.

#### CONCLUIONS

Metal-semiconductor Ag-CdS hybrid nanorods of five different lengths were synthesized using a seed-mediated growth method. The Ag:Cd(S) ratio regulated the final CdS nanorod length in the hybrid nanostructures. The Ag-CdS nanorods were applied as photocatalysts for methyl orange degradation. The catalytic activity of the nanorods were dependent on the rod length. The sample of 72.1 nm nanorods exhibited an average rate constant of 0.95 min<sup>-1</sup>, which is 29 times higher than that of the 25.0 nm sample. Time-dependent PL decays revealed that charge-separated state emission was promoted in the 59.8 and 72.1 nm Ag-CdS nanorods, in which high efficiency was also observed. This phenomenon suggests that promoting charge-separated formation is critical for improving the efficiency of photocatalysts. Understanding the physical processes in these hybrid structures provides guidance on fine-tuning their morphology for photocatalytic applications.

#### ASSOCIATED CONTENT

**Supporting Information**. The Supporting Information is available free of charge on the ACS

Publications website at DOI:

TEM images of nanostructures, optical images of Ag-CdS nanorods solution, catalytic

performance evaluation, additional experimental details, other factors that impacted Ag-CdS

nanorod synthesis, and time-dependent PL decay fitting details.

**AUTHOR INFORMATION** 

**Corresponding Author** 

\*Department of Chemistry, University of Connecticut, 55 North Eagleville Road, Storrs, CT

USA 06269-3060. jing.zhao@uconn.edu.

**Author Contributions** 

YW and JZ conceived the project and designed the experiments. YW carried out all the synthesis,

material characterization, photocatalytic measurements, UV-vis and PL spectra measurements,

and data analysis. HNN and AWM prepared the Cd precursors. YS, TM and JZ measured and

analyzed the PL decays. The manuscript was written through contributions of all authors. All

authors have given approval to the final version of the manuscript.

**Funding Sources** 

NSF CHE-1554800; CHE-2144787

ACKNOWLEDGMENT

JZ and TM acknowledge partial financial support from the National Science Foundation

(CAREER Award CHE-1554800 and CHE-2144787) for this work.

19

#### REFERENCES

- (1) Fujishima, A.; Honda, K. Electrochemical Photolysis of Water at a Semiconductor Electrode. *Nature* **1972**, *238* (5358), 37–38. https://doi.org/10.1038/238037a0.
- (2) Wang, L.; Zhao, J.; Liu, H.; Huang, J. Design, Modification and Application of Semiconductor Photocatalysts. *J. Taiwan Inst. Chem. Eng.* **2018**, *93*, 590–602. https://doi.org/10.1016/j.jtice.2018.09.004.
- Zhang, L.; Mohamed, H. H.; Dillert, R.; Bahnemann, D. Kinetics and Mechanisms of Charge Transfer Processes in Photocatalytic Systems: A Review. *J. Photochem. Photobiol. C: Photochem. Rev.* 2012, 13 (4), 263–276. https://doi.org/10.1016/j.jphotochemrev.2012.07.002.
- (4) Ani, I. J.; Akpan, U. G.; Olutoye, M. A.; Hameed, B. H. Photocatalytic Degradation of Pollutants in Petroleum Refinery Wastewater by TiO2- and ZnO-Based Photocatalysts: Recent Development. *J. Clean. Prod.* **2018**, *205*, 930–954. https://doi.org/10.1016/j.jclepro.2018.08.189.
- (5) Tee, S. Y.; Win, K. Y.; Teo, W. S.; Koh, L.-D.; Liu, S.; Teng, C. P.; Han, M.-Y. Recent Progress in Energy-Driven Water Splitting. *Adv. Sci.* **2017**, *4* (5), 1600337. https://doi.org/10.1002/advs.201600337.
- (6) Abe, R. Recent Progress on Photocatalytic and Photoelectrochemical Water Splitting under Visible Light Irradiation. *J. Photochem. Photobiol. C: Photochem. Rev.* **2010**, *11* (4), 179–209. https://doi.org/10.1016/j.jphotochemrev.2011.02.003.
- (7) Khan, Z.; Chetia, T. R.; Vardhaman, A. K.; Barpuzary, D.; Sastri, C. V.; Qureshi, M. Visible Light Assisted Photocatalytic Hydrogen Generation and Organic Dye Degradation by CdS–Metal Oxide Hybrids in Presence of Graphene Oxide. *RSC Adv.* **2012**, *2* (32), 12122–12128. https://doi.org/10.1039/C2RA21596A.
- (8) Pesci, F. M.; Wang, G.; Klug, D. R.; Li, Y.; Cowan, A. J. Efficient Suppression of Electron–Hole Recombination in Oxygen-Deficient Hydrogen-Treated TiO2 Nanowires for Photoelectrochemical Water Splitting. *J. Phys. Chem. C* **2013**, *117* (48), 25837–25844. https://doi.org/10.1021/jp4099914.
- (9) Liu, Y. Enhancing the Photocatalytic Hydrogen Evolution Performance of a Metal/Semiconductor Catalyst through Modulation of the Schottky Barrier Height by Controlling the Orientation of the Interface. *ACS Appl. Mater. Interfaces* **2017**, *9* (14), 12494–12500. https://doi.org/10.1021/acsami.7b01428.
- (10) Žerjav, G.; Zavašnik, J.; Kovač, J.; Pintar, A. The Influence of Schottky Barrier Height onto Visible-Light Triggered Photocatalytic Activity of TiO2 + Au Composites. *Appl. Surf. Sci.* **2021**, *543*, 148799. https://doi.org/10.1016/j.apsusc.2020.148799.
- (11) Arshad, M. S.; Trafela, Š.; Rožman, K. Ž.; Kovač, J.; Djinović, P.; Pintar, A. Determination of Schottky Barrier Height and Enhanced Photoelectron Generation in Novel Plasmonic Immobilized Multisegmented (Au/TiO2) Nanorod Arrays (NRAs) Suitable for Solar Energy Conversion Applications. *J. Mater. Chem. C* **2017**, *5* (40), 10509–10516. https://doi.org/10.1039/C7TC02633A.
- (12) Mokari, T.; Rothenberg, E.; Popov, I.; Costi, R.; Banin, U. Selective Growth of Metal Tips onto Semiconductor Quantum Rods and Tetrapods. *Science* **2004**, *304* (5678), 1787–1790. https://doi.org/10.1126/science.1097830.

- (13) Dutta, S. K.; Mehetor, S. K.; Pradhan, N. Metal Semiconductor Heterostructures for Photocatalytic Conversion of Light Energy. *J. Phys. Chem. Lett.* **2015**, *6* (6), 936–944. https://doi.org/10.1021/acs.jpclett.5b00113.
- (14) Wang, S.-J.; Zhang, X.-Y.; Su, D.; Yan, X.; Zhou, H.-L.; Xue, X.-M.; Wang, Y.-F.; Zhang, T. Enhanced Photocatalytic Reactions via Plasmonic Metal-Semiconductor Heterostructures Combing with Solid-Liquid-Gas Interfaces. *Appl. Catal.* **2022**, *306*, 121102. https://doi.org/10.1016/j.apcatb.2022.121102.
- (15) Jen-La Plante, I.; Habas, S. E.; Yuhas, B. D.; Gargas, D. J.; Mokari, T. Interfacing Metal Nanoparticles with Semiconductor Nanowires. *Chem. Mater.* **2009**, *21* (15), 3662–3667. https://doi.org/10.1021/cm900775w.
- (16) Naskar, S.; Schlosser, A.; Miethe, J. F.; Steinbach, F.; Feldhoff, A.; Bigall, N. C. Site-Selective Noble Metal Growth on CdSe Nanoplatelets. *Chem. Mater.* **2015**, *27* (8), 3159–3166. https://doi.org/10.1021/acs.chemmater.5b01110.
- (17) Wu, K.; Chen, Z.; Lv, H.; Zhu, H.; Hill, C. L.; Lian, T. Hole Removal Rate Limits Photodriven H2 Generation Efficiency in CdS-Pt and CdSe/CdS-Pt Semiconductor Nanorod–Metal Tip Heterostructures. *J. Am. Chem. Soc.* **2014**, *136* (21), 7708–7716. https://doi.org/10.1021/ja5023893.
- (18) Manna, G.; Bose, R.; Pradhan, N. Photocatalytic Au–Bi2S3 Heteronanostructures. *Angew. Chem. Int. Ed.* **2014**, *53* (26), 6743–6746. https://doi.org/10.1002/anie.201402709.
- (19) Amirav, L.; Alivisatos, A. P. Photocatalytic Hydrogen Production with Tunable Nanorod Heterostructures. *J. Phys. Chem. Lett.* **2010**, *I* (7), 1051–1054. https://doi.org/10.1021/jz100075c.
- (20) Banin, U.; Ben-Shahar, Y.; Vinokurov, K. Hybrid Semiconductor–Metal Nanoparticles: From Architecture to Function. *Chem. Mater.* **2014**, *26* (1), 97–110. https://doi.org/10.1021/cm402131n.
- (21) Chen, S.; Thota, S.; Reggiano, G.; Zhao, J. Generalized Seeded Growth of Ag-Based Metal Chalcogenide Nanorods via Controlled Chalcogenization of the Seeds. *J. Mater. Chem. C* **2015**, *3* (45), 11842–11849. https://doi.org/10.1039/C5TC02904J.
- (22) Shen, C.; Hui, C.; Yang, T.; Xiao, C.; Tian, J.; Bao, L.; Chen, S.; Ding, H.; Gao, H. Monodisperse Noble-Metal Nanoparticles and Their Surface Enhanced Raman Scattering Properties. *Chem. Mater.* **2008**, *20* (22), 6939–6944. https://doi.org/10.1021/cm800882n.
- (23) Wang, X.; Chen, S.; Thota, S.; Wang, Y.; Tan, H.; Tang, M.; Quan, Z.; Zhao, J. Anisotropic Arm Growth in Unconventional Semiconductor CdSe/CdS Nanotetrapod Synthesis Using Core/Shell CdSe/CdS as Seeds. *J. Phys. Chem. C* **2019**, *123* (31), 19238–19245. https://doi.org/10.1021/acs.jpcc.9b05456.
- (24) Shi, X.; Zhao, J.; Wang, Y.; Mason, R. P. The Transformation of Inorganic and Methylmercury in the Presence of L-Cysteine Capped CdSe Nanoparticles. *Front. Environ. Sci.* **2021**, *2*.
- (25) Dey, P. Ch.; Das, R. Enhanced Photocatalytic Degradation of Methyl Orange Dye on Interaction with Synthesized Ligand Free CdS Nanocrystals under Visible Light Illumination. *Spectrochim. Acta A Mol. Biomol. Spectrosc.* **2020**, *231*, 118122. https://doi.org/10.1016/j.saa.2020.118122.
- (26) Kgatle, M.; Sikhwivhilu, K.; Ndlovu, G.; Moloto, N. Degradation Kinetics of Methyl Orange Dye in Water Using Trimetallic Fe/Cu/Ag Nanoparticles. *Catalysts* **2021**, *11* (4), 428. https://doi.org/10.3390/catal11040428.

- (27) Alvi, M. A.; Al-Ghamdi, A. A.; Zulfequar, M. Synthesis and Characterization of Cadmium Chalcogenide Semiconductor Quantum Dots Based Thin Film. *J. Nanoelectron. Optoelectron.* **2016**, *11* (5), 656–661. https://doi.org/10.1166/jno.2016.1938.
- (28) Masumoto, Y.; Umino, H.; Sun, J.; Suzumura, E. Enhanced Electron Spin Rotation in CdS Quantum Dots. *Phys. Chem. Chem. Phys.* **2015**, *17* (38), 25278–25282. https://doi.org/10.1039/C5CP04256A.
- (29) Sumanth Kumar, D.; Jai Kumar, B.; Mahesh, H. M. Chapter 3 Quantum Nanostructures (QDs): An Overview. In *Synthesis of Inorganic Nanomaterials*; Mohan Bhagyaraj, S., Oluwafemi, O. S., Kalarikkal, N., Thomas, S., Eds.; Micro and Nano Technologies; Woodhead Publishing, 2018; pp 59–88. https://doi.org/10.1016/B978-0-08-101975-7.00003-8.
- (30) Wu, K.; Zhu, H.; Liu, Z.; Rodríguez-Córdoba, W.; Lian, T. Ultrafast Charge Separation and Long-Lived Charge Separated State in Photocatalytic CdS–Pt Nanorod Heterostructures. *J. Am. Chem. Soc.* **2012**, *134* (25), 10337–10340. https://doi.org/10.1021/ja303306u.
- (31) Kader, S.; Al-Mamun, Md. R.; Suhan, Md. B. K.; Shuchi, S. B.; Islam, Md. S. Enhanced Photodegradation of Methyl Orange Dye under UV Irradiation Using MoO3 and Ag Doped TiO2 Photocatalysts. *Environ. Technol. Innov.* **2022**, *27*, 102476. https://doi.org/10.1016/j.eti.2022.102476.
- (32) Yan, S. C.; Li, Z. S.; Zou, Z. G. Photodegradation of Rhodamine B and Methyl Orange over Boron-Doped g-C3N4 under Visible Light Irradiation. *Langmuir* **2010**, *26* (6), 3894–3901. https://doi.org/10.1021/la904023j.
- (33) Rasamani, K. D.; Li, Z.; Sun, Y. Significant Enhancement of Photocatalytic Water Splitting Enabled by Elimination of Surface Traps in Pt-Tipped CdSe Nanorods. *Nanoscale* **2016**, 8 (44), 18621–18625. https://doi.org/10.1039/C6NR06902A.

## **TOC GRAPHIC**

